Heliyon 10 (2024) e37943

Contents lists available at ScienceDirect

Heliyon

journal homepage: www.cell.com/heliyon

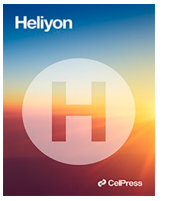

Research article

Facile Biogenic synthesis of Europium doped lanthanum silicate nanoparticles as novel supercapacitor electrodes for efficient energy storage applications

S.A. Al-Ghamdi [a], Syed Khasim [a,*], A.A.A. Darwish [a], Taymour A. Hamdalla [a], Marwah Alsharif [a], Meshari M. Aljohani [b], Mohammad Hussain [a], K. Fathihy [c]

[a] *Advanced Materials Research Laboratory, Department of Physics, Faculty of Science, University of Tabuk, Tabuk 71491, Saudi Arabia*
[b] *Department of Chemistry, Faculty of Science, University of Tabuk, Tabuk 71491, Saudi Arabia*
[c] *Department of Physics, Faculty of Science, Ain Shams University, Cairo, Egypt*

ARTICLE INFO

Keywords:
Lanthanum silicates
Eu^{3+}
XRD
DRS
Cyclic voltammetry
Galvanostatic charge discharge
Supercapacitor

ABSTRACT

In this work, we demonstrated for the first time, use of Europium doped lanthanum silicate nanoparticles (LS NPs) as electrodes for supercapacitor applications. Europium (Eu^{3+}) doped (5 mol%) LS NPs were synthesized by green solution combustion method using Mexican mint leaf extracts. Various analytical techniques such as High-Resolution Transmission Electron Microscopy (HRTEM), Selected Area Diffraction (SAED), Powder X-ray Diffraction (PXRD), Fourier Transform Infra-Red Spectroscopy (FTIR) and Diffuse Reflectance Spectroscopy (DRS) techniques were used to confirm the morphological and structural characteristics of the synthesized nanoparticles. The HRTEM and SAED patterns confirms the formation of NPs having agglomerated structure with a particle size less than 50 nm. The PXRD patterns reveals crystalline cubic structure for the NPs. Further, the FT-IR spectra reveal the successful doping of Europium in Lanthanum Silicate NPs. The DRS (Diffuse Reflectance Spectroscopy) studies confirm the reduced band gap for Europium (Eu^{3+}) doped (5 mol%) LS NPs. Cyclic voltametric and electrochemical impedance spectroscopy experiments were performed in an alkaline medium to compare the electrochemical activity of Eu^{3+} doped LS NPs with that of their undoped counterpart. The Eu^{3+} doped (5 %) LS NPs electrodes attained a specific capacitance of 373.3 Fg^{-1} at a current density of 0.5 Ag^{-1} in comparison to pure LS NPs which is about 267 Fg^{-1}. The long-term stability of the Eu^{3+} doped (5 %) LS NPs electrodes show excellent stability up to 4000 cycles of operation in comparison pure LS NPs electrodes. Doping of Eu^{3+} had a favourable effect on the conductivity and electrochemical activity of LS NPs. Due to favourable green combustion synthesis, superior electrochemical performance, these Eu^{3+} doped LS NPs could be potential materials for new generation supercapacitors in energy storage applications.

1. Introduction

The Nanoparticles (NPs) distinctive optical, chemical, physical, mechanical, electrical, and radiation-detection capabilities make them useful in a wide variety of applications, including medical imaging systems, flat-panel displays, electroluminescent and

* Corresponding author.
E-mail addresses: s.rasool@ut.edu.sa, syed.pes@gmail.com (S. Khasim).

https://doi.org/10.1016/j.heliyon.2024.e37943
Received 18 May 2024; Received in revised form 12 September 2024; Accepted 13 September 2024
Available online 16 September 2024

optoelectronic devices [1]. Nowadays, the rare earth-doped lanthanum silicates are attracting a lot of attention because of their remarkable electro-optical, photo-electric, nonlinear, and piezo-electric capabilities, as well as their exceptional chemical and physical stability [2]. Many different methods exist for synthesizing these silicates, including the following: the oxalate synthetic route, the combustion method, the wet chemical method, the solid-state reaction method, the citric-gel method, the optical floating zone method, the reaction-sintering method, the coprecipitation/calcination method, the microwave-assisted solvothermal method and many more [3–7]. Supercapacitors, often referred to as electrochemical capacitors or ultracapacitors, are rechargeable energy storage devices that store energy as charge on the electrode surface or subsurface layer after converting chemical energy into electrical energy through electrochemical reactions. Supercapacitors may produce high power because of the ease with which they release energy from the electrode surface, in contrast to batteries that store energy in bulk material. This is made possible by the charge being stored on the electrode surface. Because the charging and discharging process takes place on the electrode surface rather than causing significant structural alterations to electroactive materials, supercapacitors have exceptional cycling ability. Supercapacitors, which currently fall between electrochemical batteries and conventional capacitors, are therefore seen as a promising alternative to batteries, particularly for applications requiring maximum power, long cycle life, operational stability, fast charge-discharge time, low level of heating, appropriate dimension/weight, and low cost [8–12]. They are also seen as a viable replacement for batteries in the areas of load levelling and electrical energy storage devices.

Supercapacitors (SCs), with their higher capacity and high-power density at lower cost, have been acknowledged as a significant potential and extended cycle life/energy storage device for the next generation. Based on how they are built and stored, capacitors are divided into three categories: electrochemical, electrostatic, and electrolytic. The first generation of electrostatic capacitors, they are made up of two additional metallic plates that are spaced apart by air or an insulating material like mica, wax, ceramic and plastic parts, etc. The dielectric medium of the second-generation capacitors is supplemented with electrolytic content. The conducting electrolyte and metal foil functions as an anode (positive electrode) and cathode (negative electrode) of the dielectric medium, respectively [13,14]. By using an etching technique, a thin oxide layer has been added to the anode surface, serving as a dielectric layer to prolong the charge's duration. At that point, the capacitance of a standard electrolytic capacitor can increase to millifarads. The third generation of capacitors was constructed by using ceramic material combined with fine ferroelectric nano particles. Although these are employed in intricate electronic circuits, military-grade applications need the robust and durable capacitors that are designed with higher capacitance.

Tender perennial of the Lamiaceae family, Mexican mint (Plectranthus amboinicus, syn. Coleus aromaticus) is grown as a decorative pot plant in Japan [15–18]. The southern and eastern regions of Africa were home to this species. Its pleasant scent and ease of proliferation by cuttings have led to its widespread cultivation in recent times. Several nanoparticles have been synthesized in the recent past using Mexican mint as a primary source [19,20]. Synthesis of novel nanoparticles/nanocomposites using biological methods has been recently emerged as a cost-effective and efficient strategies to prepare the electrodes for energy storage applications [21–23].

Si, one of the most fascinating inorganic multifunctional materials, that has been extensively applied in diverse applications including sensors, electronics and opto-electronics [24,25]. In last few years, Silicon based nanomaterials and their composites have been widely used in energy storage and conversion [26,27]. In comparison to comparison to commercially available graphite materials, Si exhibits much higher reversible capacities due to their high theoretical capacity (such as 4.4 Ah g^{-1} for a $Li_4.4Si$ form) and are considered as the next-generation electrode materials (anodes) for energy storage [28]. Yet, Si or Silicate based materials undergoes drastic volume expansion issue during the continuous charge–discharge cycles, that leads to the pulverization of Si products and results in rapid decrease of reversible capacity [29]. Furthermore, the typical electroconductivity hinders their performance in practical energy storage applications [30]. Hence, these silicates are modified to form suitable composite material and further doping by rare earth materials. Hao Wan et al. and others, their advantages and have discussed in detail about the structural, physical and chemical features of various silicate materials suitable for energy conversion and storage, their advantages and drawback as well as suitable remedies [31–33].

In this work we report the facile biological synthesis of Europium (Eu^{3+}) nanoparticles using Mexican mint extracts. The Lanthanum silicate NPs were synthesized by combustion technique and doped with (Eu^{3+}) nanoparticles. These Eu^{3+} doped Lanthanum Silicate NPs were characterized by several analytical methods to study their morphological, structural and chemical features. The electrochemical performance of the fabricated electrodes based on Eu^{3+} doped Lanthanum Silicate NPs were examined through cyclic voltammetry (CV), Galvanostatic charge-discharge (GCD), impedance spectroscopy (EIS) analysis in 1M KOH electrolyte. The specific capacitance of the novel fabricated electrodes was examined and their stability was tested for 4000 cycles of charge-discharge cycles.

2. Experimental

2.1. Preparation of plant extract

Mint leaves collected, weighted (10 gm) and washed with distilled water to remove the impurities. Washed leaves boiled for about 15 min with 100 ml distilled water. Boiled Extract cooled and filtered through Whatman filter paper. Filtered, obtained plant extract used for the synthesis of LNPs nanoparticles, extract stored in refrigerator for further study.

2.2. Preparation of LNPs

10 mmol solution of the Lanthanum silicate were prepared in the distilled water and the prepared solution reduced with the prepared plant extract with 9:1 ratio. Prepared 10 mmol solution of the metal precursor were keep at 60^{o}C under constant stirring, as the solution temperature is reached at 60^{o}C plant extract is added dropwise to the reaction and then stand the reaction for 2 h with constant stirring and heating. Formation of NPs was confirm by the change in color of the reaction solution and UV characterization study, synthesized NPs washed several time with distilled water and ethanol. Particles were dried in hot air oven at 50–60^{0}C and further characterization were done.

2.3. Synthesis of Eu^{3+} (5 mol%) doped LS NPs

The Eu^{3+} (5 mol%) doped LS NPs were synthesized using the green solution combustion process. A stoichiometric amount of Lanthanum nitrate ($La(NO_3)_3.6H_2O$: 99.99 %, Sigma Aldrich Ltd.), Europium nitrate ($Eu(NO_3)_3$, 99 %, Sigma Aldrich Ltd.), fumed silica, and Mexican mint leaf extract in a Petri dish with doubled distilled water, ensuring an oxidizer-to-fuel ratio of 1 [34]. Afterwards, the uniform reaction mixture is introduced in a hot furnace that has been preheated and kept at a temperature of approximately 450 $\pm$ 10 °C to form a foam like mass. At first, the solution boils, turning it into a see-through gel. Then reaction mixture undergoes dehydration and smouldering, with liberation of large quantity of gaseous products leaving behind the white powder. The whole process only takes around 10 min, and the exothermic combustion process supplies all of the energy needed for the synthesis. Using an agate mortar and pestle, the product was ground into a fine powder. In addition, the crystallinity was enhanced by calcining the sample at 950 °C for 3 h. The above procedure was repeated for preparing the pure LS NPs sample without Eu^{3+} for comparative purposes and flowchart of synthesis is shown in Fig. 1.

2.4. Characterizations

PXRD was used to describe the phase formation of the powder sample using an X-ray diffractometer (Shimadzu) that used CuKα (1.541 Å) radiation at 50 kV and 20 mA while scanning at a rate of 2 min per minute through a nickel filter. To examine the surface

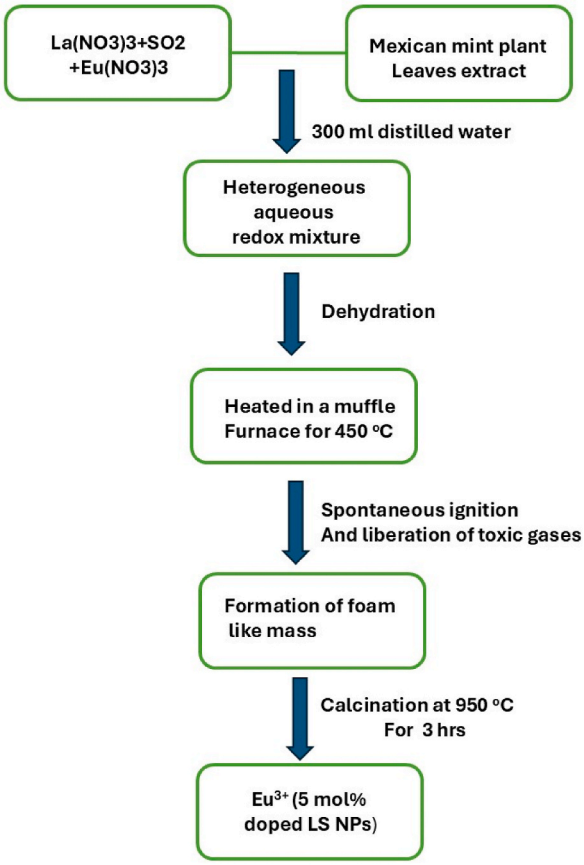

Fig. 1. Flow chart for the preparation of Eu^{3+} (5 mol%) doped lanthanum silicate NPs.

morphology, we employed a JEOL JEM-2100 EDS (accelerating voltage up to 200 kV, LaB6 filament) with a 1.5 Å TEM resolution. Various chemical and functional groups present in the obtained nano ferrites was analyzed through Fourier Transform Infrared Spectroscopy (FTIR) (Thermo Nicolet, Avatar 370 -India). The optical properties in terms of optical absorption for the synthesized ferrites was investigated using UV–visible spectrometry (Perkin Elmer-Canada).

2.5. Preparation of working electrode for electrochemical studies

Working electrode was fabricated using graphite powder, synthesized LS NPs (pure and Eu^{3+} doped) and PTFE solution in the ratio of 15:70:15 % (0.075 g: 0.350 g: 0.075 g). After that, a nickel mesh was attached onto the sheet, to form a highly conductive surface. To further enhance contact, the glued electrodes were pressed for 3 min at 20 MPa. To facilitate a strong connection between the electrodes and the electrolyte, a 30-min soak in 1 M KOH was carried out prior to their use. The electrode and wire on the circuit's negative side were insulated with Teflon tape. A detailed flow chart and schematic representation of work carried out in this study is illustrated in Fig. 2.

3. Results and discussion

3.1. PXRD studies

Fig. 4a displays the Rietveld refining pattern for doped LS NPs. The Thomson–Cox–Hasting pseudo-voigt function and the FULL-PROF programme were utilised to fit the various parameters. Software called Diamond was used to extract the potential packing diagram of LS NPs. For the cubic phase of LS NPs, the fitting parameters (Rp, Rwp, and α2) shows that the refined and observed PXRD patterns coincide fairly well. The current sample's GOF (Goodness of Fitting), which is determined by GOF = Rwp/Rexp, was found to be approximately 0.95, indicating that the experimental and theoretical plots fit the data well [34].

As illustrated in Fig. 3, the PXRD of LS NPs doped with Eu^{3+} was produced via green solution combustion method with mexican mint as fuel and it was then calcined at 950 °C for 3 h. The JCPDS card No. 53–0291, space group P_63/m, point group symmetry D_2h, and hexagonal ox apatite phase are all well indexed with all the prominent characteristic peaks of the PXRD pattern [35]. The Debye-Scherrer formula (eqn-1) is used to determine crystallite size of NPs [36].

where λ-wavelength of X-rays, β-Full width at half maximum (FWHM) of XRD peaks and the average crystallite size was obs**erve**d in the range of 30 nm.

Structural parameters of LS NPs like Inter planar spacing, volume, number of unit cells (n) in the particle (considering it to be spherical in shape), micro strain, dislocation density, x-ray density, specific surface area, Stress (σ) and stacking fault (SF) were calculated for the present material using the following relations (eqns (2)–(10)).

$$\frac{1}{d^2}=\frac{4}{3}\left[\frac{h^2+hk+l^2}{a^2}\right]+\frac{l^2}{c^2}-----\tag{2}$$

$$V=\frac{\sqrt{3}}{2}a^2c=0.866a^2c-----\tag{3}$$

$$n=\frac{4}{3\pi\left(\frac{D}{2V}\right)}-----\tag{4}$$

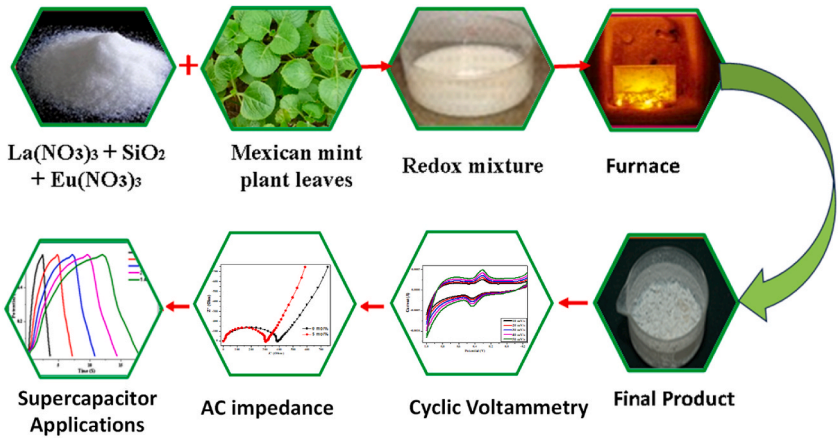

Fig. 2. Schematic representation of the work carried out in this study.

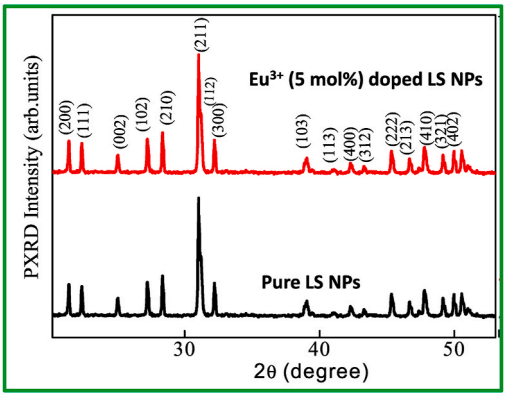

Fig. 3. PXRD spectra of pure and Eu^{3+} (5 mol%) doped LS NPs.

$$\varepsilon = \frac{\beta \, COS \, \theta}{4} - - - - - - \quad (5)$$

$$D_x = \frac{16M}{Na^2c} - - - - - \quad (6)$$

$$\delta = \frac{1}{D^2} - - - - - \quad (7)$$

$$S = 6/D_x D - - - - - \quad (8)$$

$$\sigma_{stress} = \varepsilon E - - - - - \quad (9)$$

$$SF = \left[\frac{2\pi^2}{45\sqrt{(3 \, tan \, \theta)}}\right] - - - - - \quad (10)$$

Where M; molecular mass, N; Avogadro's number (6.0223 x 10^{23} particles mol^{-1}), a; lattice constant, and D represent the number of $La_{10}Si_6O_{27}$molecules per unit cell, 'E'; the elastic constant or generally known as Young's modulus of the material. Young's modulus of the $La_{10}Si_6O_{27}$ is 122 GPa. All the calculated values are given in Table 1.

$$\beta \cos \theta = \frac{\mathbf{0.9\lambda}}{\boldsymbol{D}} + \mathbf{4\varepsilon} \, \boldsymbol{sin} \, \boldsymbol{\theta} - - - - - - - - - \quad (11)$$

where 'ε'; the strain associated with the nanoparticles [36]. The above equation represents a straight line between '4sinθ' (x-axis) and 'βcosθ' (y-axis) as shown in Fig. 4b. The slope of the line gives the strain and intercept of this line on y-axis gives crystallite size (D) around 28.20 nm.

3.2. Transmission electron Microscopy (TEM) analysis

TEM investigations were conducted on LS NPs doped with 5 mol% Eu^{3+} along with SAED, HRTEM, and the images are shown in Fig. 5(a–c). All the particles are strongly agglomerated, as expected of combustion-synthesized products (Fig. 5(a–c)). Fig. 5d shows a clear ring pattern in the chosen region electron diffraction (SAED) of LS NPs. According to the HRTEM (Fig. 5e), the interplanar distance 'd' was approximately 0.20 nm, which is very near to the 0.20 nm value for the (210) planes Fig. 6a shows the purity of the prepared nanomaterials and Fig. 6b shows average distribution of crystallite size [37].

Table 1
Estimated crystallite size and strain values of $La_{10}Si_6O_{27}$:Eu^{3+} nanoparticles.

Sample	Parameters								
	D (nm)	d (nm)	V (Å^3)	n x 10^{20}	$D_x x 10^4$ (kgm^{-3})	δ x 10^{15} ($kgm^{-3})^{-2}$	ε x10^{-3}	σ x 10^8 (Pa)	SF
Eu^{3+} (5 mol%) doped LS NPs ((300) plane)	30	0.39	562.12	6.244	2485	1.6773	1.781	227.932	0.4733

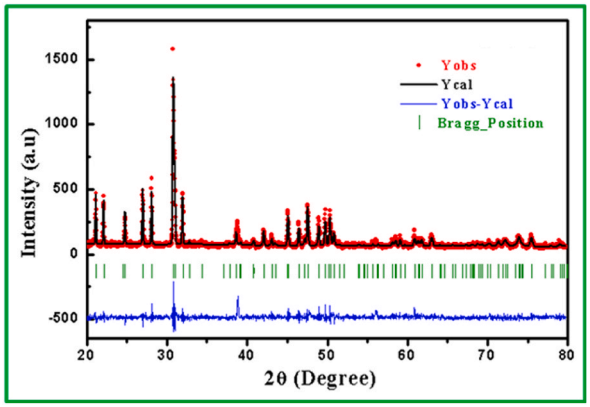

Fig. 4a. Rietveld refinement of LS NPs.

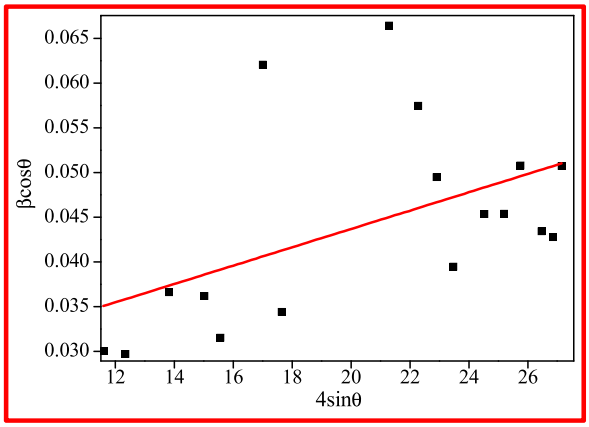

Fig. 4b. W-H Plot of Eu^{3+} (5 mol%) doped LS NPs. Further, crystallite size of the doped nanoparticles prepared by combustion method is calculated using the W-H plots (using eqn-11).

3.3. FT-IR studies

FTIR spectra of undoped and (5 mol%) Eu^{3+} doped LS NPs recorded in the wave number range of 400–4000 cm^{-1} were presented in Fig. 7. The observed band at 645 cm^{-1} is attributed to the La–O bond formation. A band appeared at 854 cm^{-1} is attributed to Si–O–Si asymmetric stretch, while a band at 1063 cm^{-1} corresponds to SiO_6 group. IR bands at 1500 cm^{-1} is due to the stretching vibration of the surface silanol hydrogen bond (Si–OH) to molecular water and the peak at 2353 cm^{-1} corresponds to stretching vibration of O–H group [38,39]. Addition of Eu^{3+} into the lattice of LS NPs has not affected the FTIR spectra of LS NPs significantly except for the slight change be due to structural modifications in SiO_6 network upon Eu^{3+} doping.

3.4. Raman spectroscopy

The Raman spectroscopy was used to analyze the microstructures of pure Lanthanum NPs and Eu^{3+} doped Lanthanum NPs. The Raman spectra of both the samples were depicted in Figure-8. The Raman spectroscopy was effectively analyzed using the optical phonon vibrations of the molecules present in the sample. As it can be seen from the figure that the intense peaks in the Raman spectra confirms the formation of Lanthanum Silicate NPs. The high intensity Raman absorption at characteristic 656 cm^{-1} confirms the cubic phase of the crystal lattice as observed in case of XRD analysis. The characteristic broad peak around 656 cm^{-1} also indicates presence of Bg phonon mode in the LS NPs, whereas the peaks at 438 cm^{-1} and 481 cm^{-1} indicates the presence of two Ag phonon modes. The distortions in the Raman signal as observed in the spectra mainly arises due to randomly distributed vacancies in LS NPs. The characteristic peak around 656 cm^{-1} also indicates the RE-O bond and presence of oxygen vacancies in the sample. The doping of Eu^{3+} results in slight increase in peak intensity as well as broadening of characteristic peaks associated with LS NPs.

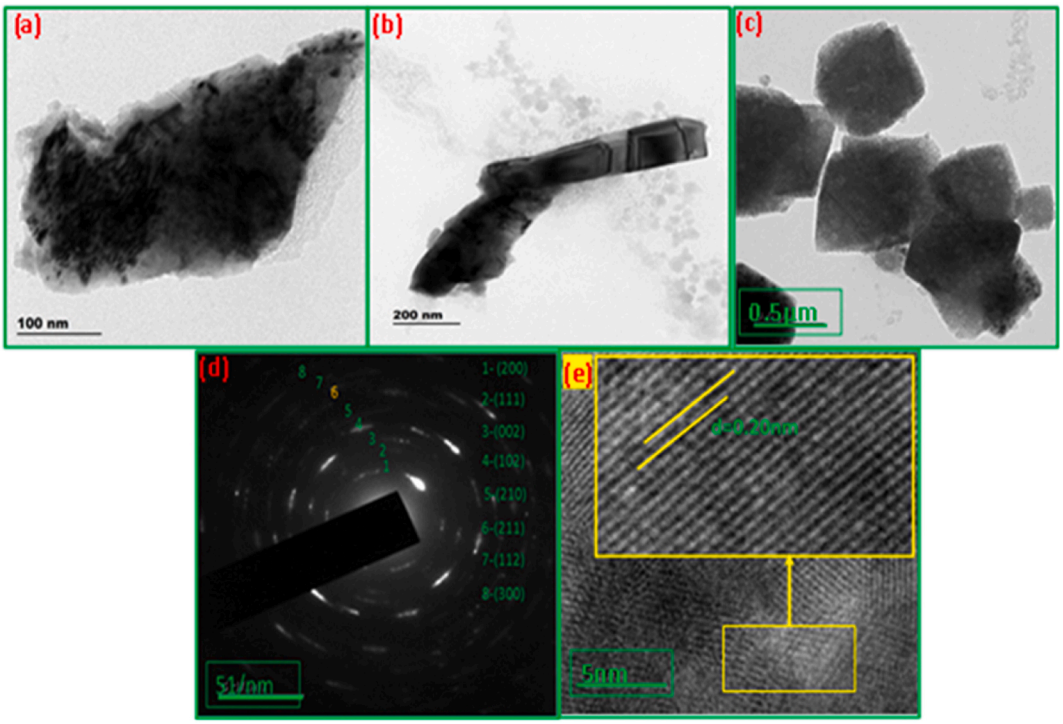

Fig. 5. (a, b & C) TEM images (d) SAED pattern and (e) HRTEM of Eu^{3+} (5 mol%) doped LS NPs.

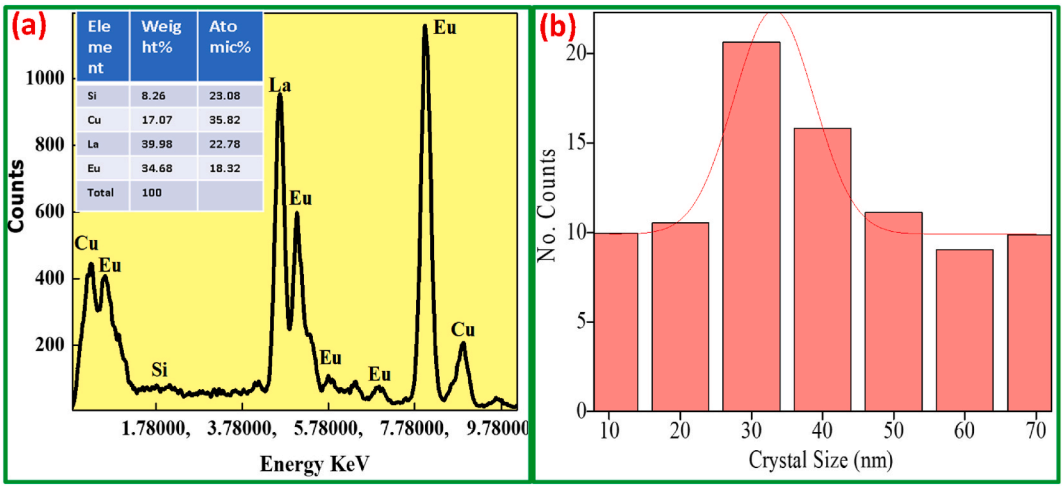

Fig. 6. (a) EDAX b) Histogram of the Eu^{3+} (5 mol %) doped LS NPs.

3.5. *Diffuse Reflectance Spectroscopy (DRS)*

The absorption characteristics of crystalline, powdered and nanostructured materials can be accurately through spectral bands using DRS. The spectra show modifications when the spectrometer beam hits the sample and reflects, scatters and transmits through the substance. In Fig. 9 (a), diffuse reflectance spectra of pure and Eu^{3+} (5 mol%) doped LS NPs were shown. The absorption coefficient, denoted as F(R), is used to plot the spectra. The optical energy band gap was calculated from the spectra via the Kubelka-Munk equation (eqn-12) [38].

$$F(R_\infty)h\nu = C(h\nu - E_G)^n \tag{12}$$

Where, F (R_∞)-Kubelka-Munk function, $h\nu$-photon energy, C-constant, E_g-Optical energy band gap, n-constant associated with different

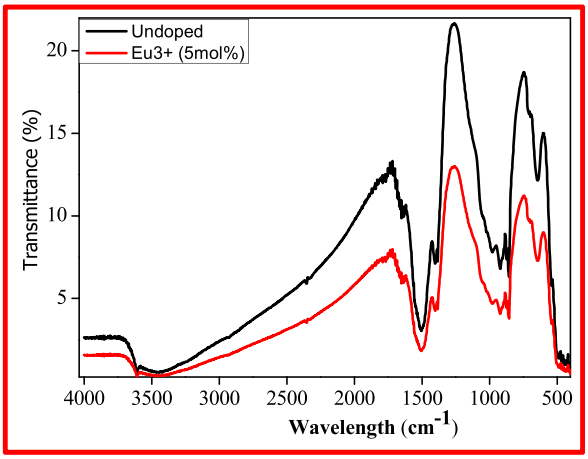

Fig. 7. FT-IR spectra of undoped and (5 mol%) Eu^{3+} doped LNs.

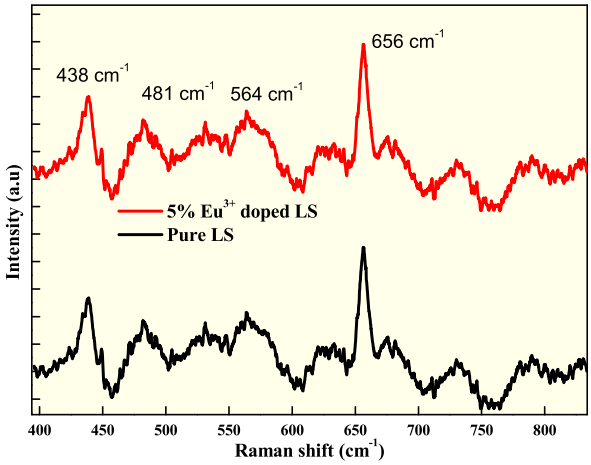

Fig. 8. Raman spectra of undoped and (5 mol%) Eu^{3+} doped LNs.

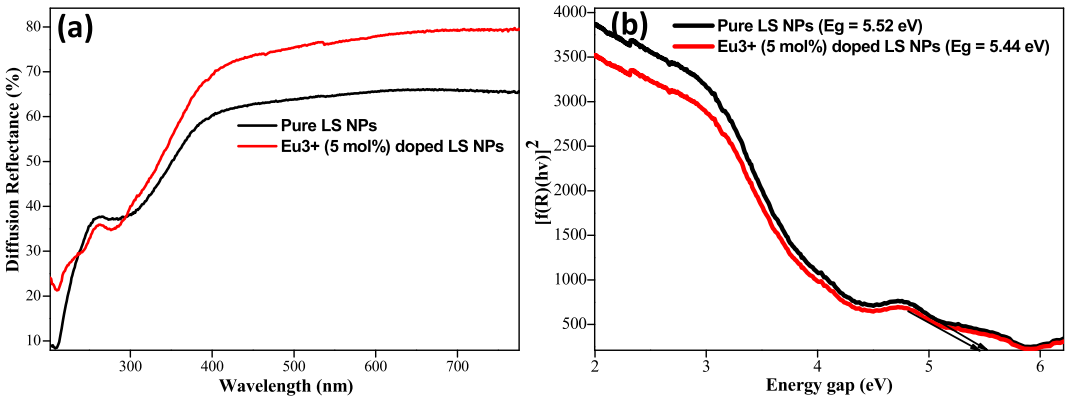

Fig. 9. (a) DRS and (b) Energy band gap spectra of pure and Eu^{3+} (5 mol%) doped LS NPs.

kinds of transitions viz., $n = 1/2$ for a direct allowed transition, $n = 2$ for an indirect allowed transition, $n = 3/2$ for a direct forbidden transition and $n = 3$ for an indirect forbidden transition. Eu^{3+} doped LS NPs may absorb UV and visible areas of solar radiation, as indicated clearly in Fig. 9 (b), where the optical band gap of the resulting NPs was found to be 5.52 and 5.44 eV, respectively, acquired by extrapolating the line to zero.

3.6. Electrochemical studies

Electrode reversibility, charge efficacy, and charge-discharge properties of an electrode can be investigated using cyclic voltametric curves. A range of scan rates were employed for the nanomaterial electrodes containing both pure and 5 % Eu^{3+} doped LS NPs (as shown in Fig. 10-a, b). Potential range from −0.25 V to 1.0 V was used for the CV studies against Ag/AgCl in 1M KOH electrolyte. These results are compared with the redox behaviour of pure and 5 % Eu^{3+} doped LS electrodes are crucial to the current study and shows significant redox peaks. The CV curves indicate a pseudo capacitor behaviour than an actual electrical double-layer capacitor [39]. The additive-treated electrodes have a higher capacity because La^0 can be entirely oxidised to La^{3+} in this mechanism [40].

Using eqn 13 and 14 for reversible processes developed by Randles-Sevcik [41], the height current is shown as

$$ip = 2.69 \times 10^5 \times n^{3/2} \times A \times D^{1/2} \times C_0 \times v^{1/2} \quad (13)$$

The number of electrons transferred, rate of diffusion, size of the electrode, initial concentration and the scanning rate can be represented using the variables n, D, A, C_o and v respectively.

$$C_o = \frac{\rho}{m} - - - - - \quad (14)$$

The density and the molar mass of pure and 5 % Eu^{3+} doped LS electrodes were signified by ρ and M.

The relationship between ip and $v^{1/2}$ are shown in Fig. 11. Hydrogen diffusion appears to be a limiting factor in the electrode reactions of pure and 5 % Eu^{3+} doped LS electrodes, as seen via linear relationship between ip and $v^{1/2}$. 5 % Eu^{3+} doped LS electrode material (5.717×10^{-5} cm^2 s^{-1}) showed an enhanced proton transport coefficient than the pure LS electrode (2.2322×10^{-6} cm^2s^{-1}), according to our results.

The Electrochemical Impedance Spectroscopy (EIS) for all the samples were recorded in the frequency range 100 KHz-0.1 Hz. The EIS spectra of pure and 5 % Eu^{3+} doped LS electrodes are shown in Fig. 12, Warburg resistance is depicted by a slope in the spectra at low frequencies, while charge transfer resistance is shown at high frequencies [42–45]. Since the electrode resistance drops dramatically in presence of 5 % Eu^{3+} doped LS electrode, it is clear that this electrochemical reaction occurs prior to pure LS electrode. The increased electrochemical activity of 5 % Eu^{3+} doped LS electrode compared to pure LS electrode is revealed by lower Rct and higher Cdl values (Table 2) [46]. This result indicates that the presence of 5 % Eu^{3+} doped LS electrode improves the charge transfer process and its efficiency.

In circuit, W represents Warburg part that is within the low frequency region of impedance spectra; generally, for a plate-like electrode, the Warburg slope is about 45^o and is proportional to $1/CD^{1/2}$ (C is the concentration of diffusive species and D is the hydrogen diffusion co-efficient). However, for porous electrodes and for those systems which involve a series of reactions; this relation does not hold true [47]. The charge transfer resistance (Rct) and double layer capacitance (C) values measure the two-dimensional figure at high frequencies as observed in the resistance plot (Fig. 12). A rise in the capacitance and lowering of the charge transfer resistance on addition of Eu^{3+} unambiguously manifests the superiority of LS electrode with 5 % Eu^{3+} additive over pure LS electrode.

Figs. 13 and 14 depicts the GCD curves for pure and 5 % Eu^{3+} doped LS electrode for the First 5, 1000th, 2000th cycles at a current density of 1 Ag^{-1}, these investigations were carried out in comparison to Ag/AgCl during 2000 cycles in potential window of 0–0.6 V. Experiments were conducted to determine the electrodes' durability, their charge-discharge functionalities. The 5 % Eu^{3+} doped LS electrode has the best cycle stability compared to the pure LS electrode (see Fig. 15).

Fig. 15 (a, b) displays the GCD curves for pure and 5 % Eu^{3+} doped LS electrodes at varying current densities. The results show that the charge-discharge curves seem more like those of a pseudo-capacitor than that of a standard electric double-layer capacitor. More energy can be stored at higher current densities as more surface area is integrated along the current-potential axis. The capacitance at each electrode was analyzed using the relation mentioned below (eqn-15) [48,49].

$$C = \frac{i\Delta t}{m\Delta V} - - - - - - \quad (15)$$

where, *i*-applied current, ΔV-potential range, Δt-time of a discharge cycle and m-mass of pure and 5 % Eu^{3+} doped LS electrode. Specific capacitance values of pure and 5 % Eu^{3+} doped LS electrodes at various current densities are shown in Table 3, it shows high-capacitance for 5 % Eu^{3+} doped LS electrode. Even after 2000 cycles of charge-discharge in 1M KOH, the 5 % Eu^{3+} doped LS electrode taken more than 90 % of its primary capacitance.

At a current density of 0.5A/g, pure and 5 % Eu^{3+} doped LS electrodes are shown to be stable up to 2000 charge-discharge cycles (Fig. 16). After 2000 cycles, the voltage is seen to drop significantly in case of pure LS NPs, whereas for the 5 % Eu^{3+} doped LS electrodes, the decrease is marginal. After the completion of 4000 cycles of charge-discharge, the 5 % Eu^{3+} doped LS electrodes show a capacitance retention rate of nearly 90 %. The improved stability of the electrodes is attributed to the doping of Eu^{3+} in LS NPs. The electrochemical supercapacitor performance of the Eu^{3+} doped LS electrodes investigated in the present study are compared with the previously published literature on Lanthanum related materials and is depicted in table-4.

4. Conclusions

Using Mexican mint leaves extract as a fuel, nanocrystalline pure and Eu^{3+} (5 mol%) doped lanthanum silicate NPs were synthesized through solution combustion approach, exhibiting remarkable physicochemical properties and enhanced electrochemical performances. PXRD determined the NPs crystallinity, phase purity, and crystallite size, revealing that the samples contain a hexagonal

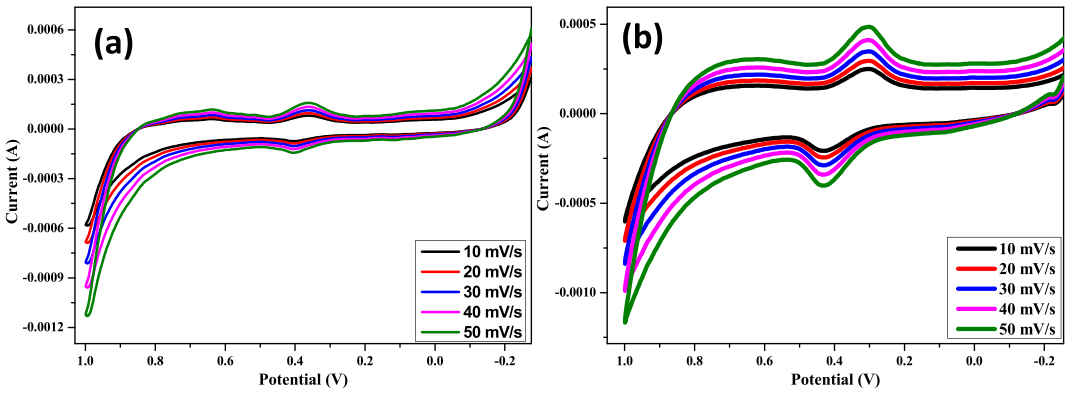

Fig. 10. CV of (a) pure LS and (b) 5 % Eu^{3+} doped LS electrodes.

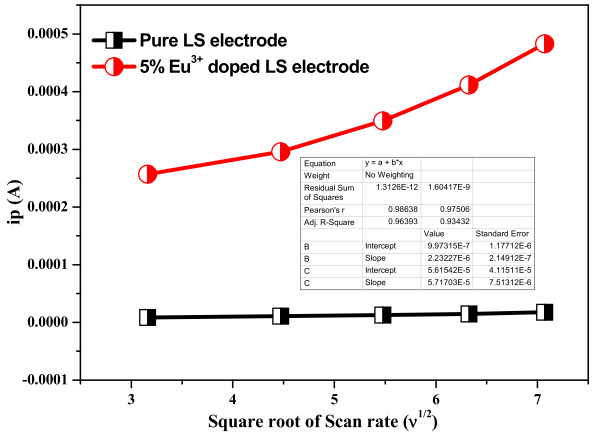

Fig. 11. Relationship between cathodic peak current (i_p) and square root of the scan rate ($v^{1/2}$) of pure and 5 % Eu^{3+} doped LS electrodes.

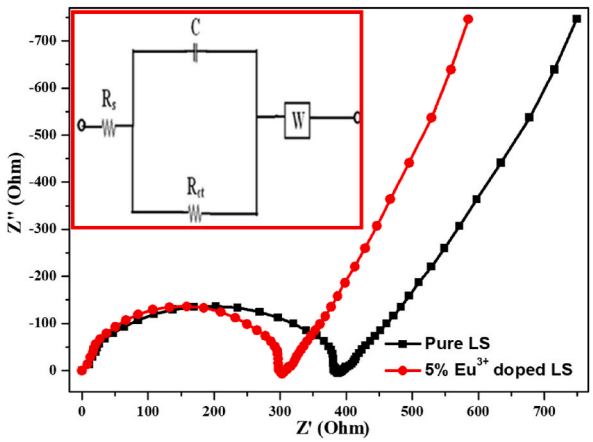

Fig. 12. Nyquist plot of pure LS and 5 % Eu^{3+} doped LS electrodes with fitted circuit.

oxapatite phase with crystallite sizes 30 nm. The electrochemical performance of pure LS NPs and Eu^{3+} doped (5 %) LS NPs were analyzed through CV, GCD, EIS and stability studies. The Eu^{3+} doped (5 %) LS NPs electrodes attained a specific capacitance of 373.3 Fg^{-1} at a current density of 0.5 Ag^{-1} in comparison to pure LS NPs which is about 267 Fg^{-1}. The long-term stability of the Eu^{3+} doped (5 %) LS NPs electrodes show excellent stability up to 4000 cycles of operation in comparison pure LS NPs electrodes. Eu^{3+} doped (5 %) LS NPs electrodes retain >90 % of its capacitance after 4000 cycles of operation. Due to cost effective biosynthesis, excellent electrochemical properties and long-term stability, these Eu^{3+} doped LS NPs electrodes could be potentially used in the fabrication of

Table 2
Circuit parameters fitted with the EIS data.

Name of the Electrode	Rs (Ω)	Rct (Ω)	Cdl (F)	Proton diffusion coefficient (D) $cm^2\ s^{-1}$
Pure LS electrode	16.1	0.00395	0.000650	2.2322×10^{-6}
5 % Eu^{3+} doped LS electrode	12.2	0.00299	0.000932	5.717×10^{-5}

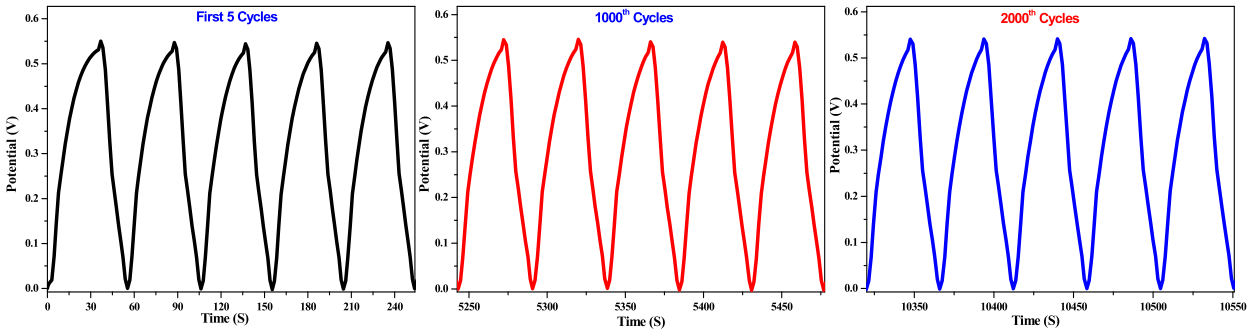

Fig. 13. First 5, 1000th, 2000th GCD cycles of pure LS electrode.

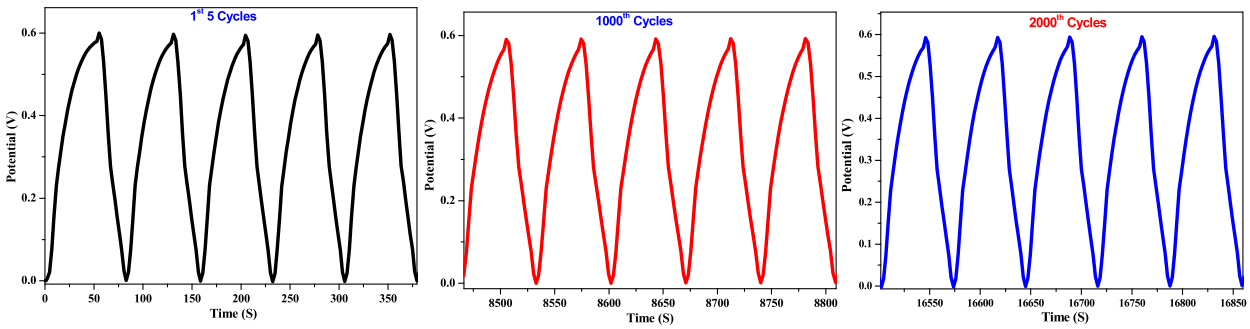

Fig. 14. First 5, 1000th and 2000th GCD cycles of 5 % Eu^{3+} doped LS electrode.

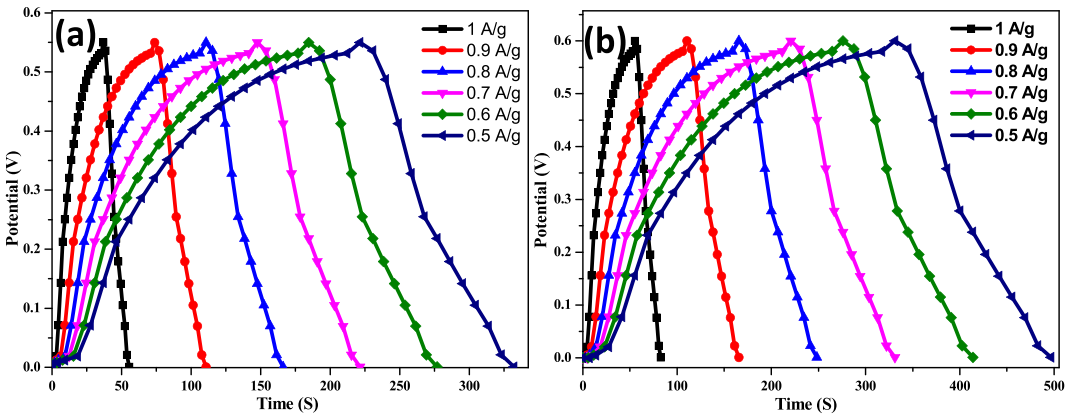

Fig. 15. GCD curves of (a) pure and (b) 5 % Eu^{3+} doped LS electrodes at various current densities.

Table 3
Specific capacitance values in various current densities of pure and 5 % Eu^{3+} doped LS electrodes.

Current density	Specific capacitance (F/g)	
	Pure LS	5 % Eu^{3+} doped LS
1 A/g	86.8	121.7
0.9 A/g	158.6	216.1
0.8 A/g	214.1	296.3
0.7 A/g	250.3	344.7
0.6 A/g	261.9	365.8
0.5 A/g	267.4	373.3

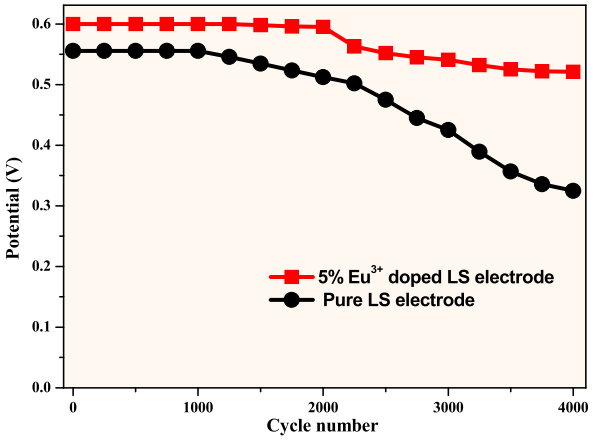

Fig. 16. The variation of potential with cycle numbers at a current density of 0.5 A/g of the pure and 5 % Eu^{3+} doped LS electrodes.

Table-4
Comparison of Specific capacitance with previous literature Lanthanum NPs.

Sl.No	Material/Synthesis	Electrolyte	Specific Capacitance	Reference
1	RGO/$LaAlO_3$ (Hydrothermal)	1M KOH	283 Fg^{-1} @0.5 Ag^{-1}	[50]
2	$LaMnO_3$ (Hydrothermal)	1 M KOH	73 Fg^{-1} @ 0.5Ag^{-1}	[51]
3	$LaNiO_3$	6 M KOH	422 F g−1 @ 1 A g−1	[52]
4	$LaFeO_3$	LiOH	16.43 F g−1	[53]
	$LaCro_3$		24.40 F g−1	
5	$LaMnO_3$/RGO/PANI	3 M KOH	111 F g^{-1} @ 2.5 A g^{-1}	[54]
6	La_1−XSrXMnO_3	1 M KOH	102 F g^{-1} @ 1 A g^{-1}	[55]
7	Eu^{3+} doped (5%Mol) Lanthanum Silicate NPs (Green Synthesis)	1M KOH	373.3 Fg^{-1} @ 0.5 Ag^{-1}	Present work

supercapacitors. Further, detailed studies on effect of Eu^{3+} concentrations in LS NPs may lead to stabilizing these electrode materials for technological applications.

Data availability

All the data related to the present research is included in this manuscript.

CRediT authorship contribution statement

S.A. Al-Ghamdi: Project administration, Methodology, Funding acquisition, Conceptualization. **Syed Khasim:** Writing – review & editing, Writing – original draft, Project administration, Methodology, Investigation, Data curation. **A.A.A. Darwish:** Validation, Software, Project administration, Conceptualization. **Taymour A. Hamdalla:** Writing – review & editing, Methodology, Investigation, Data curation. **Marwah Alsharif:** Validation, Supervision, Software, Methodology. **Meshari M. Aljohani:** Writing – review & editing, Software, Resources, Conceptualization. **Mohammad Hussain:** Visualization, Validation, Supervision, Investigation. **K. Fathihy:** Software, Methodology, Data curation, Conceptualization.

Declaration of competing interest

The authors declare that they have no known competing financial interests or personal relationships that could have appeared to influence the work reported in this paper.

Acknowledgements

The authors would like to acknowledge financial support for this work, from the Deanship of Scientific research (DSR), University of Tabuk, Tabuk, Saudi Arabia, under Grant No.S-1443-0020.

References

[1] T. Grzyb Tymiński, Enhancement of the up-conversion luminescence in $LaVO_4$nanomaterials by doping with M^{2+}, M^{4+} ($M^{2+} = Sr^{2+}$, Ba^{2+}, Mg^{2+}; $M^{4+} = Sn^{4+}$) ions, J. Alloy Compd. 782 (2019) 69–80.
[2] L. Tarpani Bellacanzone, P. Luigi Gentili, L. Latterini, Effects of glutathione on the luminescent behavior of CdSe-nanocrystals, J. Lumin. 226 (2020) 117513.
[3] Devender Singh, Suman Sheoran, Vijeta Tanwar, Europium doped silicate phosphors: synthetic and characterization techniques, Advanced Materials Letters 8 (5) (2017) 656–672.
[4] R. Farma, M. Deraman, A. Awitdrus, I.A. Talib, E. Taer, N.H. Basri, J.G. Manjunatha, M.M. Ishak, B.N. Dollah, S.A. Hashmi, Preparation of highly porous binderless activated carbon electrodes from fibres of oil palm empty fruit bunches for application in supercapacitors, Bioresour. Technol. 132 (2013) 254–261.
[5] R. Kotz, M. Carlen, Principles and applications of electrochemical capacitors, Electrochim. Acta 45 (2000) 2483–2498.
[6] Zahra Heydariyan, Rozita Monsef, Elmuez A. Dawi, Masoud Salavati-Niasari, $EuMnO_3$/$EuMn_2O_5$/MWCNT nanocomposites: insights into synthesis and application as potential materials for development of hydrogen storage capacity, Fuel 351 (2023) 128885.
[7] J. Ma, Y.-z. Dong, L. Wang, P. Yu, H.-j. Yan, C.-g. Tian, J.-h. Li, H.-g. Fu, In–situ molten salt template strategy for hierarchical 3D porous carbon from palm shells as advanced electrochemical supercapacitors, ChemistrySelect 1 (2016) 2167–2173.
[8] Syed Khasim, Yogendra Kumar Misra, Nacer Badi, Apsar Pasha, Mohana Lakshmi, Fabrication of high performance flexible supercapacitors using secondary doped PEDOT-PSS:Graphene nanocomposite films for large area solid state devices, RSC Adv. 10 (2020) 10526–10539.
[9] S. Saranya, R.K. Selvan, N. Priyadharsini, Synthesis and characterization of polyaniline/MnWO4 nanocomposites as electrodes for pseudocapacitors, Appl. Surf. Sci. 258 (2012) 4881–4887.
[10] Syed Khasim, Apsar Pasha, Mohana Lakshmi, Paneerselvam Chellasamy, Murugan Kadarkarai, A.A.A. Darwish, Taymour A. Hamdalla, S.A. Al-Ghamdi, S. Alfadhli, Post treated PEDOT-PSS films with excellent conductivity and optical properties as multifunctional flexible electrodes for possible optoelectronic and energy storage applications, Opt. Mater. 125 (2022) 112109.
[11] J. Xia, F. Chen, J. Li, N. Tao, Measurement of the quantum capacitance of graphene, Nat. Nanotechnol. 4 (2009) 505–509.
[12] Syed Khasim, Apsar Pasha, Mohana Lakshmi, Chellasamy Panneerselvam, Mohammad Fahad Ullah, A.A.A. Darwish, Taymour A. Hamdalla, S. Alfadhli, S.A. Al-Ghamdi, Synthesis of g-C_3N_4/CuO nanocomposite as a supercapacitor with improved electrochemical performance for energy storage applications, Int. J. Electrochem. Sci. 17 (2022) 220838.
[13] H. Liu, P. He, Z. Li, Y. Liu, J. Li, A novel nickel-based mixed rare-earth oxide/activated carbon supercapacitor using room temperature ionic liquid electrolyte, Electrochim. Acta 51 (2006) 1925–1931.
[14] S. Faraji, F.N. Ani, Electroless nano zinc oxide–activate carbon composite supercapacitor electrode, J. Electroceram. (2016) 1–7.
[15] W. Amaki, N. Yamazaki, M. Ichimura, H. Watanabe, Effects of light quality on the growth and essential oil content in sweet basil, Acta Hortic. 907 (2011) 91–94.
[16] K. Besser, A. Harper, N. Welsby, I. Schauvinhold, S. Slocombe, Y. Li, R.A. Dixon, P. Broun, Divergent regulation of terpenoid metabolism in the trichomes of wild and cultivated tomato species, Plant Physiol 149 (1) (2009) 499–514.
[17] M. Ebisawa, K. Shoji, M. Kato, K. Shimomura, F. Goto, T. Yoshihara, Effects of supplementary lighting of UV-B, UV-A and blue light during the night on growth and coloring in red-leaf lettuce, J. SHITA 20 (2008) 158–164.
[18] D. Ioannidis, L. Bonner, C.B. Johnson, UV-B is required for normal development of oil glands in Ocimum basilicum, L. (sweet basil). Ann. Bot. 90 (4) (2002) 453–460.
[19] J.L. Hernández-Pinero, M. Terrón-Rebolledo, R. Foroughbakhch, et al., Effect of heating rate and plant species on the size and uniformity of silver nanoparticles synthesized using aromatic plant extracts, Appl. Nanosci. 6 (2016) 1183–1190.
[20] M.W. Alam, N. Allag, M. Utami, M. Waheed-Ur-Rehman, M. Al Saleh Al-Othoum, S. Sadaf, Facile green synthesis of α-bismuth oxide nanoparticles: its photocatalytic and electrochemical sensing of glucose and uric acid in an acidic medium, J. Compos. Sci. 8 (2024) 47.
[21] S.A. Al-Ghamdi, A.A. A Darwish, Taymour A. Hamdallah, Mohamed E. Elnair, Ahmed Al-Atawi, Syed Khasim, Biological synthesis of novel carbon quantum dots using halimeda opuntia green algae with improved optical properties and electrochemical performance for energy storage applications", Int. J. Electrochem. Sci. 18 (2023) 100102.
[22] Syed Khasim, Syed G. Dastager, Mohammed Issa Alahmdi, Taymour A. Hamdalla, Chellasamy Panneerselvam, Mohammad Basha Makandar, Novel Biogenic Synthesis of Pd/TiO@BC as an electrocatalytic and possible energy storage materials, Ceram. Int. 49 (2023) 15874–15883.
[23] Syed Khasim, Syed G. Dastager, Mohammed Issa Alahmdi, Taymour A. Hamdalla, Mohammad Fahad Ulla, Chellasamy Panneerselvam, Mohammad Basha Makandar, Green Engineered Multifunctional Cu/MnO@Biochar Nanocomposite with excellent electrochemical and catalytical performances for possible energy storage and environmental applications, Case studies in chemical and Environmental Engineering 9 (2024) 100561.
[24] J. Li, R. Li, C.H. Chiang, Y. Zhong, H. Shen, E. Song, M. Hill, S.M. Won, K.J. Yu, J.M. Baek, Y. Lee, J. Viventi, Y. Huang, J.A. Rogers, Adv. Mater. Tech. 5 (2020) 1900800.
[25] A. Qiu, P. Li, Z. Yang, Y. Yao, I. Lee, J. Ma, Adv. Funct. Mater. 29 (2019) 1806306.
[26] J. Ryu, J.H. Seo, G. Song, K. Choi, D. Hong, C. Wang, H. Lee, J.H. Lee, S. Park, Nat. Commun. 10 (2019) 2351.
[27] Y. Son, J. Ma, N. Kim, T. Lee, Y. Lee, J. Sung, S.-H. Choi, G. Nam, H. Cho, Y. Yoo, J. Cho, Adv. Energy Mater. 9 (2019) 1803480.
[28] F. Wang, G. Chen, N. Zhang, X. Liu, R. Ma, Carbon Energy 1 (2019) 219–245.
[29] F. Dai, R. Yi, H. Yang, Y. Zhao, L. Luo, M.L. Gordin, H. Sohn, S. Chen, C. Wang, S. Zhang, D. Wang, ACS Appl. Mater. Interfaces 11 (2019) 13257–13263.
[30] C.H. Jung, J. Choi, W.S. Kim, S.H. Hong, J. Mater. Chem. A 6 (2018) 8013–8020.
[31] Hao Wan, Wei Ma, Kechao Zhou, Yijun Cao, Xiaohe Liu, Renzhi Ma, Advanced silicon nanostructures derived from natural silicate minerals for energy storage and conversion, Green Energy Environ. 7 (2022) 205–220.
[32] G.G. Eshetu, E. Figgemeier, Confronting the challenges of next-generation silicon anode-based lithium-ion batteries: role of designer electrolyte additives and polymeric binders, ChemSusChem 12 (2019) 2515–2539.
[33] Xiuxia Zuo, Jin Zhu, Peter Müller-Buschbaum, Ya-Jun Cheng, Silicon based lithium-ion battery anodes: a chronicle perspective review, Nano Energy 31 (2017) 113–143.
[34] Li, W. Liu, W. Pan, Synthesis and electrical properties of apatite-type $La_{10}Si_6O_{27}$, J. Power Sources 195 (2010) 2196–2201.
[35] G.P. Darshan, H.B. Premkumar, H. Nagabhushana, S.C. Sharma, B. Daruka Prasad, S.C. Prashantha, R.B. Basavaraj, Superstructures of doped yttrium aluminates for luminescent and advanced forensic investigations, J. Alloy Compd. 686 (2016) 577–587.

[36] C.R. Ravikumar, P. Kotteeswaran, A. Murugan, V. Bheema Raju, M.S. Santosh, H.P. Nagaswarupa, H. Nagabhushana, S.C. Prashantha, M.R. Anil Kumar, K. Gurushantha, Electrochemical studies of nano metal oxide reinforced nickel hydroxide materials for energy storage applications, J. mater today proc. 4 (2017) 12205–12214.
[37] R. Naik, S.C. Prashantha, H. Nagabhushana, S.C. Sharma, B.M. Nagabhushan, H.P. Nagaswarupa, H.B. Premkumar, Low temperature synthesis and photoluminescence properties of red emitting $M_{g2}Si_{O4}:E^{3+}$nanophosphor for near UV light emitting diodes, Sensor. Actu. B Chem. 13 (2014) 140–149.
[38] S. Nakayama, Y. Higuchi, M. Sugawara, A. Makiya, M. Sakamoto, Fabrication of c-axis-oriented apatite-type polycrystalline $La_{10}Si_6O_{27}$ ceramic and its anisotropic oxide ionic conductivity, Ceram Inter 40 (2014) 1221–1224.
[39] Rozita Monsef, Masoud Salavati-Niasari, Architecturally robust tubular nano-clay grafted Li0.9Ni0.5Co0.5O2-x/LiFeO2 nanocomposites: new implications for electrochemical hydrogen storage, Fuel 332 (Part 1) (2023) 126015.
[40] C.S. McCamy, Correlated color temperature as an explicit function of chromaticity coordinates, Color Res. Appl. 17 (1992) 142–144.
[41] A.I. Inamdar, S.M. YoungSam Kim, J.H. Kim, Hyunsik Im, Hyungsang Kim, Chemically grown, porous, nickel oxide thin-film for electrochemical supercapacitors, J. Power Sources 196 (4) (2011) 2393–2397.
[42] J.D.H.B. Chen, D.H. Bradhurst, S.X. Dou, Hua-Kun Liu, Nickel hydroxide as an active material for the positive electrode in rechargeable alkaline batteries, J. Electrochem. Soc. 146 (10) (1999) 3606.
[43] A.H. Zimmerman, A.H.P.K. Effa, Discharge kinetics of the nickel electrode, J. Electrochem. Soc. 131 (4) (1984) 709.
[44] Y.W. Li, J.H. Yao, C.J. Liu, W.M. Zhao, W.X. Deng, S.K. Zhong, Effect of interlayer anions on the electrochemical performance of Al-substituted α-type nickel hydroxide electrodes, Int. J. Hydrogen Energy 35 (6) (2010) 2539–2545.
[45] C.R. Ravi Kumar, M.S. Santosh, H.P. Nagaswarupa, S.C. Prashantha, S. Yallappa, M.R. Anil Kumar, Synthesis and characterization of β-Ni $(OH)_2$ embedded with MgO and ZnO nanoparticles as nanohybrids for energy storage devices, Mater. Res. Express 4 (6) (2017) 065503.
[46] I. Inamdar, Y.S. Kim, J.S. Sohn, H. Im, Hyung Kim, D.Y. Kim, R.S. Kalubarme, C.H. Park, Supercapacitive characteristics of electrodeposited polyaniline thin films grown on indium-doped tin-oxide substrates, J. Kor. Phys. Soc. 59 (2011) 145–149.
[47] C.R. Ravikumar, M.R. Anil Kumar, H.P. Nagaswarupa, S.C. Prashantha, Aarti S. Bhatt, M.S. Santosh, Denis Kuznetsov, CuO embedded β-$Ni(OH)_2$ nanocomposite as advanced electrode materials for supercapacitors, J. Alloys and Compounds, Elsevier 738 (2018) 332–339.
[48] A.S. Manjunatha, N.S. Pavithra, M. Shivanna, G. Nagaraju, C.R. Ravi Kumar, Synthesis of Citrus Limon mediated SnO2-WO3 nanocomposite: applications to photocatalytic activity and electrochemical sensor, J. Environ. Chem. Eng. 8 (2020) 104500.
[49] Naik R. Lakshmana, T Bala Narsaiah, P. Justin, Syed Khasim, A. Naveen Kumar, N. Raghavendra, R. Ramesh, C.R. Ravikumar, Hydrothermal synthesis and characterization of nanostructured nickel vanadate for supercapacitor and photocatalytic applications, Mater. Res. Express 10 (2023) 125009.
[50] T.N. Vinuth Raj, Priya A. Hoskeri, H.B. Muralidhara, C.R. Manjunatha, K. Yogesh Kumar, M.S. Raghu, Facile synthesis of perovskite lanthanum aluminate and its green reduced graphene oxide composite for high performance supercapacitors, J. Electroanal. Chem. 858 (2020) 113830.
[51] X.W. Wanga, X. Wang, H.C. Zhang, Q.Q. Zhu, D. Zheng, L.Y. Sun, Preparation and electrochemical properties of LaMnO3 powder as a supercapacitor electrode material, Key Eng. Mater. 727 (2017) 698–704.
[52] T. Shao, H. You, Z. Zhai, T. Liu, M. Li, L. Zhang, Hollow spherical $LaNiO_3$ supercapacitor electrode synthesized by a facile template-free method, Mater. Lett. 201 (2017) 122–124.
[53] N. Arjun, G.T. Thomas, C.K. Yang, The exploration of lanthanum based perovskites and their complementary electrolytes for the supercapacitor applications, Results Phys. 7 (2017) 920–926.
[54] P.M. Shafi, V. Ganesh, A.C. Bose, LaMnO3/RGO/PANI ternary nanocomposites for supercapacitor electrode application and their outstanding performance in all-solid state asymmetrical device design, ACS Appl. Energy Mater. 1 (2018) 2802–2812.
[55] X. Lang, H. Mo, X. Hu, H. Tian, Supercapacitor performance of perovskite $La_1-xSrxMnO_3$, Dalton Trans. 46 (2017) 13720–13730.